ORIGINAL RESEARCH ARTICLE

Microstructures and Photovoltaic Properties of TiO$_2$/BiFeO$_3$ Core–Shell Nanowire Arrays

Jiahua Li[1,3] · Jizhuang He[2,3] · Sisi Li[1,3] · Yin Ren[1,3] · Ke Ding[2] · Shulin Xing[2,3] · Yunfei He[1,3] · Rongli Gao[2,3] · Chunlin Fu[2,3] ⓘ

Abstract

To address the current problem of low photoelectric conversion efficiency of BiFeO$_3$ (BFO)-based photovoltaic (PV) devices, a TiO$_2$/BFO core–shell nanowire array structure was constructed in this study based on the characteristics of excellent light reflection, stronger light-trapping effect, large specific surface area, fast transport rate of photogenerated carriers, and good energy band matching relationship. The TiO$_2$/BFO core–shell nanowire arrays were prepared by the hydrothermal and sol–gel methods. The experimental results show that the light absorption performance of the TiO$_2$/BFO core–shell nanowire arrays is significantly enhanced compared with the previously reported BFO-based ferroelectric photovoltaic (FEPV) films, and the conversion efficiency has significantly improved to 0.1177%. The intrinsic mechanism of PV enhancement of the designed TiO$_2$/BFO core–shell nanowire array structure was illustrated by combining optical absorption, carrier lifetime, and energy band structure. This study further demonstrates the potential applications of transport material/ferroelectric material core–shell nanowire array structures in PV devices.

Keywords BiFeO$_3$ · nanowire array · ferroelectric photovoltaic effect · core–shell structure

Introduction

With rapid economic development, environmental pollution caused by the large-scale use of fossil fuels threatens the safety of human life. Demand for renewable energy has become an urgent issue.[1] Solar energy is a renewable and non-polluting energy source, and it is favored for energy conversion. Solar cells that can convert solar energy into electrical power have become a research focus.[2] Silicon-based solar cells are used extensively; however, their high production costs and energy consumption are not conducive to sustainable development. Therefore, new photovoltaic (PV) materials are currently in demand.[1–3]

Owing to their low manufacturing costs and high thermal stability, ferroelectric-based PV materials have attracted considerable interest. Unlike the PV devices of conventional semiconductors, ferroelectric photovoltaic (FEPV) devices exhibit a unique PV mechanism. Notably, the open-circuit voltage (V_{oc}) of a FEPV device can be at least four orders of magnitude larger than its bandgap.[4] The built-in electric field generated by ferroelectric polarization can spread throughout the device, theoretically allowing for higher photoelectric conversion efficiency (PCE).[4] Compared to conventional FEPV materials (e.g., BaTiO$_3$,[5,6] Pb(Zr, Ti)O$_3$,[5,6] and LiNbO$_3$[6,7]), BiFeO$_3$ (BFO) with a perovskite structure is of interest because of its high responsiveness to visible light, with a relatively narrow bandgap (~2.7 eV) and large photovoltage compared to other ferroelectrics.[8] However, the photocurrent in the BFO PV devices is still low. This is probably because of the relatively insufficient optical absorption capacity and lack of effective charge transport and carrier collection.

✉ Rongli Gao
gaorongli2008@163.com

✉ Chunlin Fu
chlfu@126.com

1 School of Chemistry and Chemical Engineering, Chongqing University of Science and Technology, Chongqing 401331, China

2 School of Metallurgy and Materials Engineering, Chongqing University of Science and Technology, Chongqing 401331, China

3 Chongqing Key Laboratory of Nano/Micro Composite Materials and Devices, Chongqing 401331, China

For PV semiconductor devices, optical absorption loss includes reflection and transmission loss, mainly depending on the refractive index difference between the semiconductor material and the surrounding environment.[9] Transmission loss results primarily from the insufficient absorption capacity of the semiconductor material.[9,10] Because of their unique structural characteristics, semiconductor nanowire arrays can act as an antireflection layer in the device.[9–12] Nanowire arrays also have excellent light-trapping ability, which can extend the residence time or propagation distance of light in the material, thus improving the optical absorption capacity of the material and effectively reducing the transmission loss of the device.[13,14] The incident light bounces back and forth between the nanowires to form resonance, thus limiting the light in the nanowire arrays.

To improve carrier transport efficiency, inserting a transport layer into solar cells is essential.[15] Therefore, in this study, an electron transport layer (ETL) was introduced in ferroelectric (such as BFO) nanowire arrays, as shown in Fig. 1. These nanowire arrays have a large specific surface area, high order, good reflection reduction, and a high light concentration. Most importantly, nanowire arrays with core–shell structures have the advantages of nanowire arrays, and allow better contact between the absorbing layer and the ETL, shorten the carrier transport path, and accelerate effective carrier separation.

TiO$_2$ nanomaterials, as commonly used ETLs, have attracted considerable attention because of their non-toxicity, chemical stability, cost-effectiveness, large specific surface area, efficient carrier transport, and good light-trapping ability.[16–18] The optoelectronic properties of BFO nanoparticles were significantly improved after their growth on the surface of TiO$_2$ nanotubes.[16] Zhu et al. demonstrated that BFO growth on TiO$_2$ leads to a TiO$_2$/BFO heterojunction, which generates energy band bending at the interface.[16,19] Therefore, TiO$_2$ promotes the transfer of photoinduced electrons from the BFO layers. In other words, as an ETL, TiO$_2$ can compensate for the ability of BFO to transport photogenerated electrons. Therefore, we designed and constructed a TiO$_2$/BFO core–shell nanowire array structure to improve the PCE of BFO.

In this study, the structure of BFO thin-film solar cells was improved. The BFO absorber layer was wrapped on the surface of the transport material—TiO$_2$ nanowire arrays to construct TiO$_2$/BFO nanowire arrays with a core–shell structure. The composite structure retains the stable and spontaneous polarizable characteristics of BFO and the excellent properties of TiO$_2$ nanowire arrays, which achieve full absorption of sunlight and fast carrier transport, increase the contact area between the core and shell, and enhance the synergistic effect of the transport and absorber layers.

In this context, we considered studying the relationship between the microstructure of TiO$_2$/BFO core–shell nanowire arrays and their PV performance, for improving the PV performance of ferroelectrics.

Experimental Details

Preparation of TiO$_2$ Nanowire Arrays

First, F-doped tin oxide (FTO) conductive glass (10 mm × 10 mm × 2.2 mm) was ultrasonically treated using an ultrasonic cleaning machine. The ultrasonic cleaning solutions used were detergent, deionized water, acetone, and ethanol. Each ultrasonic step lasted 15 min.

Second, 8 mL of deionized water, 1.3 mL of alcohol, and 8 mL of hydrochloric acid were mixed, and 267 μL of butyl titanate was added to the resultant solution and stirred for 20 min to obtain the TiO$_2$ precursor solution.

Third, TiO$_2$ nanowire arrays (TNAs) were grown via a hydrothermal reaction. The prepared TiO$_2$ precursor was

Electron transport layer
Bottom electrode
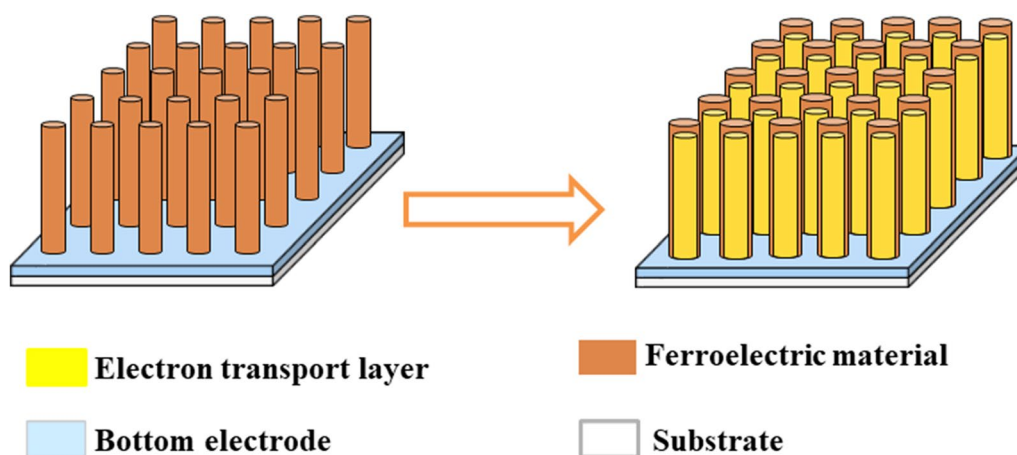**Ferroelectric material**
Substrate

Fig. 1 Schematic of the design for core–shell nanowire arrays.

poured into a reaction kettle (50 mL) with FTO conductive glass, and the hydrothermal reaction was carried out at 150°C for 6 h. After completion of the reaction, the samples were removed and washed with distilled water.

Finally, the cleaned samples were placed in a crucible and annealed at 500°C for 30 min to obtain crystallized TNAs.

Preparation of BFO Sol

The BFO absorbent layer was prepared using the sol–gel method. Bismuth(III) nitrate pentahydrate ($Bi(NO_3)_3 \cdot 5H_2O$) (5% excess $Bi(NO_3)_3 \cdot 5H_2O$, to compensate for bismuth ion volatilization at high temperatures) and iron(III) nitrate nonanhydrate ($Fe(NO_3)_3 \cdot 9H_2O$) were dissolved in 2-methoxyethanol ($C_3H_8O_2$) to prepare the 0.2 mol/L BFO sol. After the solute was dissolved, 1 mL of acetate and 2 mL of ethylene glycol were added to stabilize the sol. The reaction solution was stirred at 70°C for 3 h, and further stirred for 24 h after cooling to room temperature (25°C). Finally, the BFO sol was obtained after aging for 24 h.

Preparation of BFO Shell Layers

The BFO shell layers were prepared by dropping BFO colloids onto the TNAs, spinning at 4000 rpm for 30 s, drying at 80°C for 10 min, and annealing at 550°C for 1 h. The preparation procedures for the TiO₂/BFO core–shell nanowire arrays are shown in Fig. 2.

Characterization Methods

The crystal structure of the TiO₂ and TiO₂/BFO nanowire arrays was characterized using X-ray diffraction (XRD; Fangyuan, D2700). The surface morphology was studied using field-emission scanning electron microscopy (FESEM; JEOL, JSM-7800F). Single TiO₂/BFO nanowires were observed by transmission electron microscopy (TEM; JEOL JEM-2100F) and high-resolution transmission electron

microscopy (HRTEM), and the optical absorption characteristics of the samples were analyzed by ultraviolet–visible spectroscopy (UV–Vis; Shimadzu, UV2600i). A solar cell test system (Crowntech, *IV* Test Station 2000) was used to measure the *J–V* curves of the nanowire array solar cells in the dark and under AM 1.5G illumination with an intensity of 100 mW/cm². Time-resolved photoluminescence (TRPL) of the core–shell nanowire arrays was measured using a fluorescence spectrometer (Horiba, FluoroMax 4), and the carrier lifetime was obtained by fitting the spectrum with an exponential function. Ultraviolet photoelectron spectroscopy (UPS; Thermo Scientific, ESCALAB 250Xi) was used to measure the work function, valence band edge, and secondary electron cutoff edge of the TiO₂ and TiO₂/BFO nanowire arrays, and the energy-level structure maps and band matching of the samples were obtained via calculations.

Results and Discussion

Crystal Structures

The crystal structures of TiO₂ and TiO₂/BFO samples were studied by XRD (Fig. 3a). The crystal phase of TiO₂ is tetragonal rutile, which belongs to the *P*42/*mm* space group (JCPDS No. 75-1748).

The BFO layers crystallize well and have perovskite structures. Unlike the BFO spin-coated directly on FTO, the diffraction peaks of BFO in the TiO₂/BFO structure are generally shifted toward the right by 0.09°, mainly because the residual compressive stress between the BFO and TiO₂ nanowire arrays reduces the crystal plane spacing.[20,21] The diffraction peaks of TiO₂/BFO at 22.51°, 31.84°, 32.16°, 39.57°, 45.84°, 51.40°, and 57.25° corresponded to the (012), (104), (110), (202), (024), (116), and (300) planes of the *R*3*c* space group (JCPDS No. 86-1518), respectively. No apparent secondary phases were observed in the BFO layers. Figure 3b
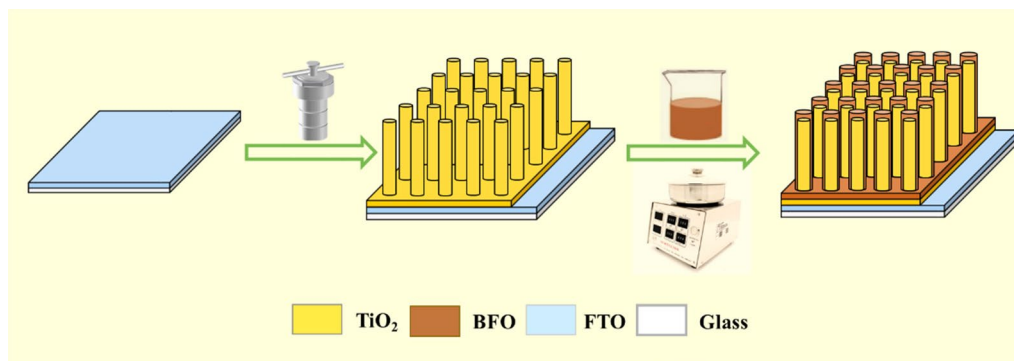

Fig. 2 Schematic of step-by-step preparation of TiO₂/BFO core–shell nanowire arrays.

shows the enlarged XRD patterns at approximately $2\theta = 31.5°–32.5°$. The characteristic peaks at 31.84° and 32.16° corresponded to the (104) and (110) planes of BFO, respectively. Comparing the XRD patterns of FTO/BFO and TiO$_2$/BFO, the half-peak width of the main diffraction peaks of BFO in TiO$_2$/BFO was wider than that of FTO/BFO under the same conditions, indicating that the grain size of BFO in the TiO$_2$/BFO structure was reduced.
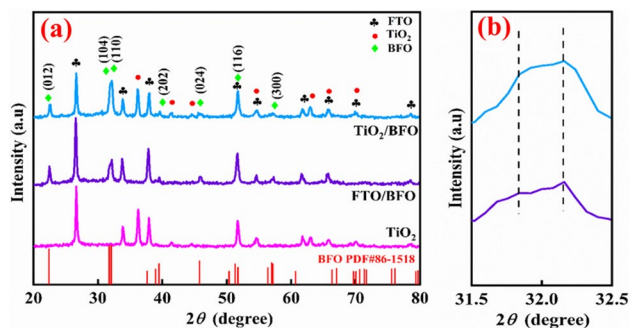
**Fig. 3** (a) XRD patterns of TiO$_2$, FTO/BFO, and TiO$_2$/BFO, (b) local amplification of (a).

Morphological Characterizations

The surface morphology of the TiO$_2$ and TiO$_2$/BFO nanowire arrays was studied by FESEM. Figure 4a and b show homogeneous vertically arranged TNAs grown on FTO/glass substrates. The inset in Fig. 4a shows the diameter distribution of TNAs. The average length and diameter of the nanowires were approximately 1.3 μm and 120 nm, respectively. Figure 4c and d show the energy-dispersive X-ray spectroscopy (EDS) images of the TNAs growing on the FTO/glass substrates. Ti and O elements are predominantly observed in the EDS images of TiO$_2$, which match with XRD results, confirming that the TNAs were successfully grown on the FTO/glass substrate.

Figure 5a and b show the nanowire array structure coated with 0.2 mol/L BFO sol on the TiO$_2$ nanowires. When the solution concentration is low, the BFO layer uniformly covers the TNAs. Figure 5c and d show the EDS images of the TiO$_2$/BFO nanowire arrays, which indirectly confirms that the BFO sol was successfully coated on the surface of the TNAs. Comparing Figs. 5 and 4, the BFO sol in Fig. 5 is uniformly coated mainly on the upper half of the TiO$_2$ nanowires, and the difficulty in uniform coating at the lower half of the nanowires could be owing to the mismatch between the colloid viscosity and sparsity of the nanowire array. This
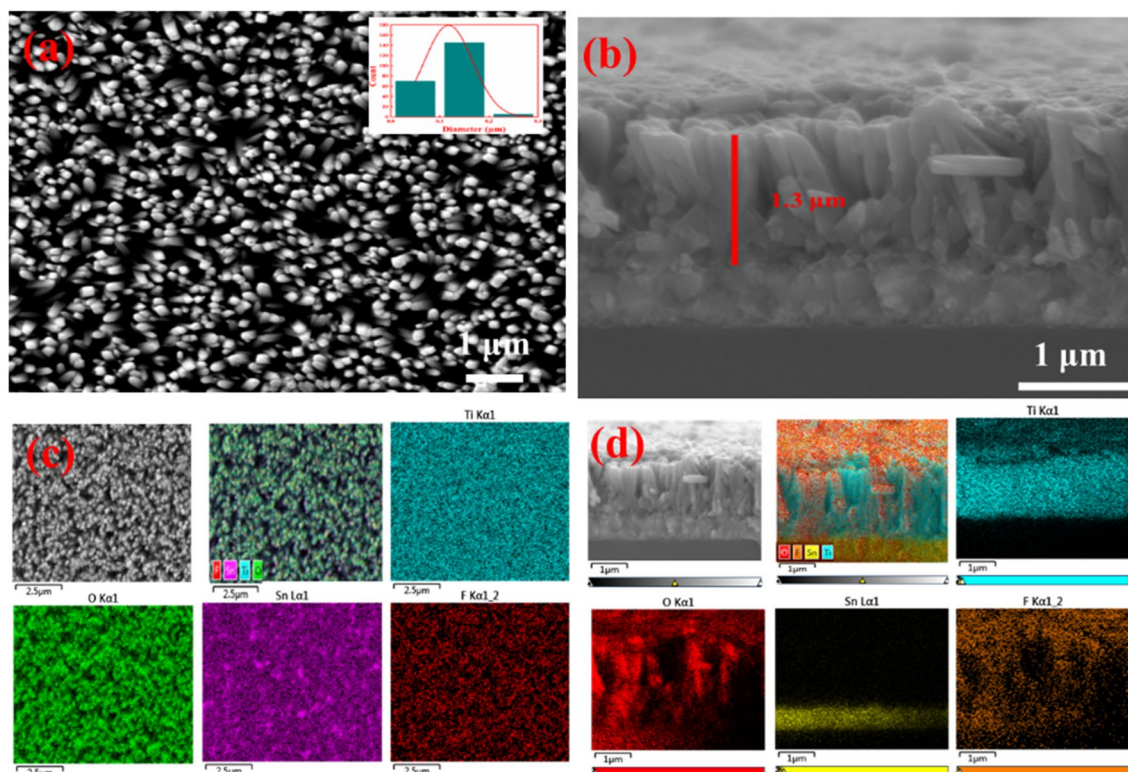
Fig. 4 Top (a) and cross-sectional views (b) and corresponding elemental distribution, (c, d) TiO$_2$ nanowire arrays. The inset of (a) shows the diameter distribution.
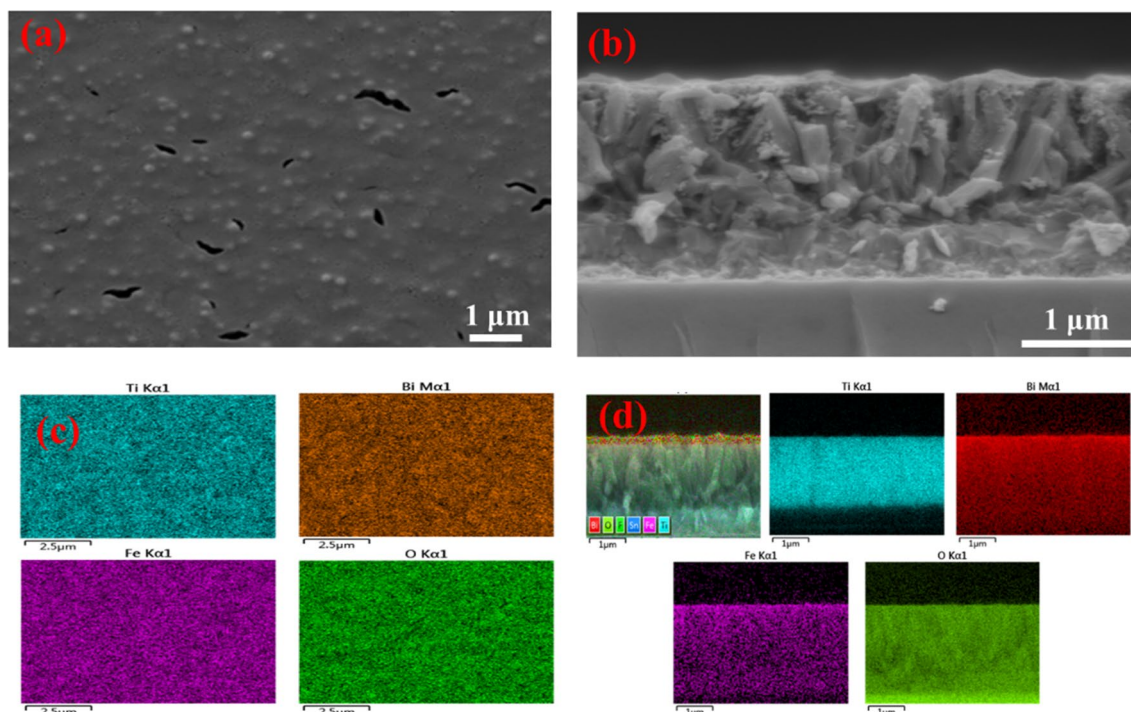
Fig. 5 Top (a) and cross-sectional views (b) and corresponding elemental distributions, (c, d) TiO$_2$/BFO core−shell nanowire arrays.

observation also provides a more meaningful reference for further improvement of the PCE of BFO-based materials. Notably, the roughness of the composite surface was greater than that of the BFO-based thin film materials after the BFO sol was coated on the TiO$_2$ nanowire array, which was beneficial for the composite material to reduce the reflection and increase the light-trapping effect, and consequently improve the light absorption aided by the nanowire array.

TEM images further confirmed the formation of core−shell nanowire arrays. As shown in Fig. 6a, BFO uniformly covered the TiO$_2$ nanowires with a diameter of approximately 140 nm. Figure 6b shows the HRTEM

images of TiO$_2$/BFO, corresponding to the lattice fringes of BFO and TiO$_2$. The measured d spacing of 0.32 nm belongs to the (110) plane of rutile TiO$_2$. The BFO shell thickness uniformly covering the TiO$_2$ surface is approximately 10 nm, (140–120)/2 = 10 and the d spacing of 0.28 nm corresponds to the (110) plane of rhombohedral BFO.
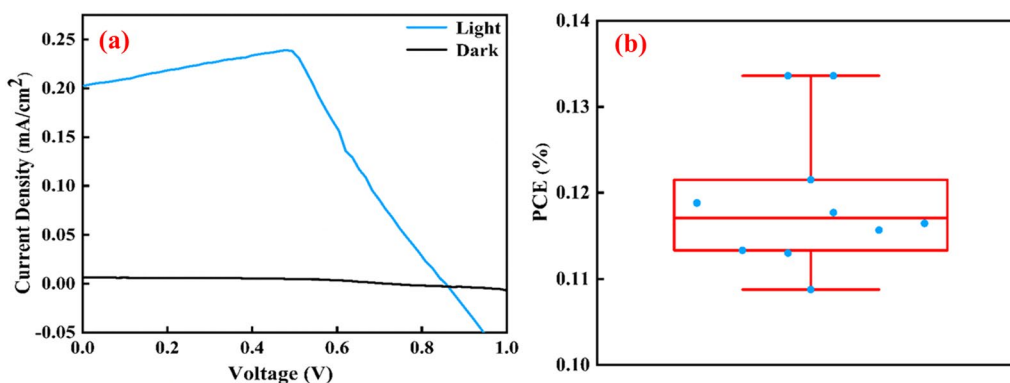
Optical Properties

The optical absorption characteristics of the TiO$_2$ and TiO$_2$/BFO nanowire arrays were characterized using a UV–Vis
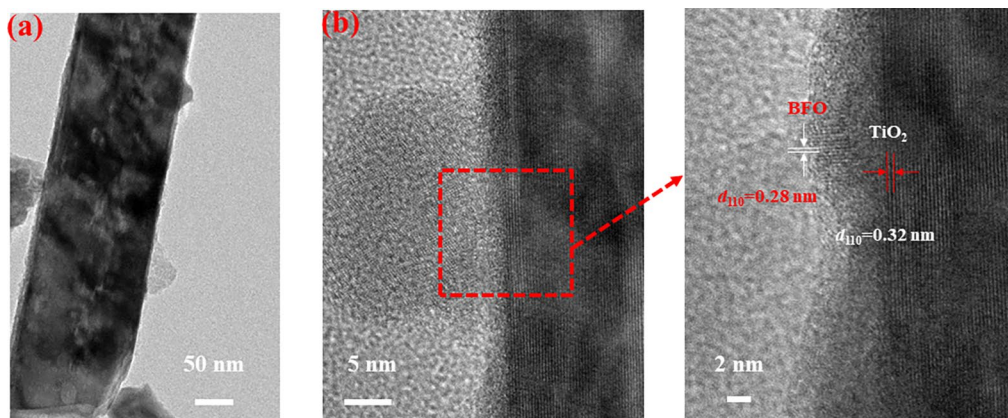
Fig. 6 TEM (a) and HRTEM (b) images of TiO$_2$/BFO core−shell nanowire.
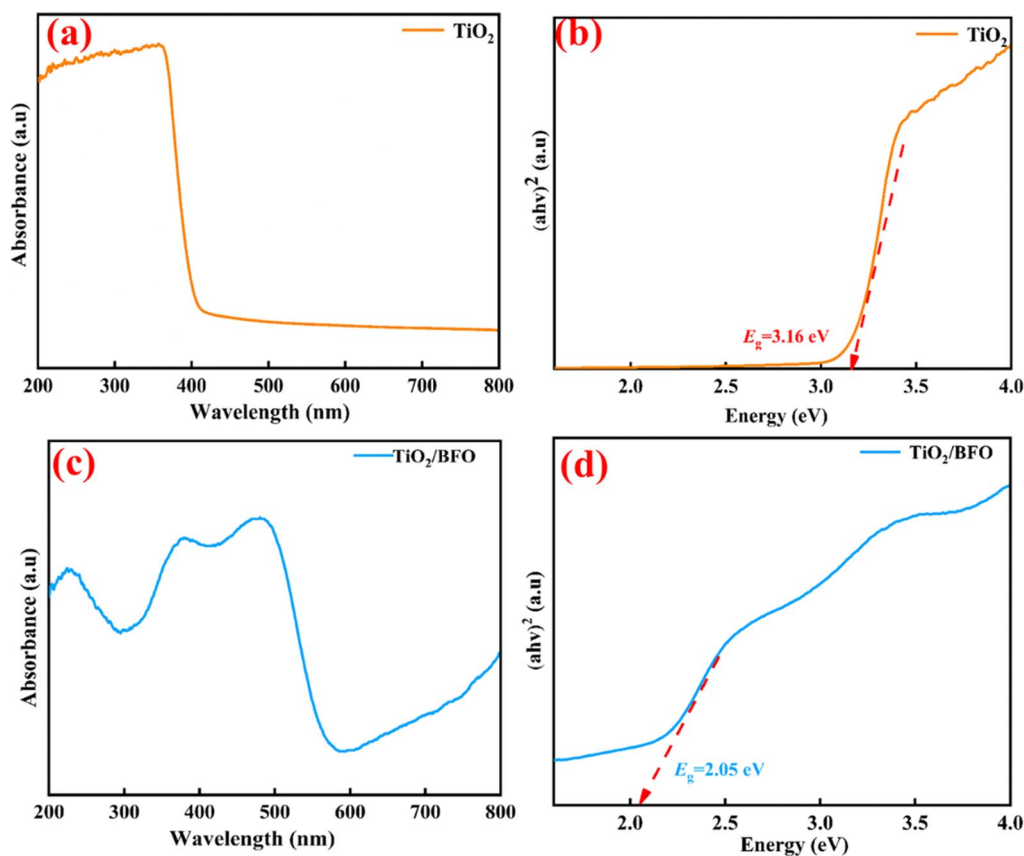
Fig. 7 Light absorption (a, c) and bandgap diagrams (b, d) of TiO_2 and TiO_2/BFO nanowire arrays.

Fig. 8 *J–V* curves (a) and box diagram of the PCE (b) of TiO_2/BFO core–shell nanowire arrays.

spectrophotometer. Figure 7a shows the optical absorption performance of the TiO_2 nanowire arrays with the highest absorption peak at 380 nm. The main optical absorption range of the TiO_2 nanowire arrays was 200–380 nm. As shown in Fig. 7c, the TiO_2/BFO nanowire arrays exhibited good optical absorption properties. The main optical absorption range of the TiO_2/BFO nanowire arrays was 200–520 nm, and a wider absorption range than that of TiO_2 nanowire arrays indicates that the spin coating of BFO

materials on TiO_2 nanowire arrays is beneficial for improving the absorption performance of single TiO_2 materials. The absorption spectrum of TiO_2/BFO is not smooth compared to that of TiO_2, and several fluctuating absorbing segments are observed, mainly because the utilization of visible light is improved after BFO is spin-coated on the TiO_2 nanowire arrays. The rough surface reduces the reflection of light and forms multiple trapping effects, which in turn enhances the absorption of light.

Simultaneously, the main light absorption range of TiO$_2$/BFO nanowire arrays is 200–520 nm, which is wider than that reported in the literature for BFO films on FTO/glass (320–500 nm).[22] The absorption at 200–380 nm is mainly attributed to the TiO$_2$ nanowire arrays, and that at 380–800 nm is mainly ascribed to TiO$_2$/BFO nanowire arrays.

Combined with the top view of BFO coated on the TiO$_2$ nanowire arrays in Fig. 5, the surface roughness is much greater than that of BFO-based films because of the roughness and sparsity of the TiO$_2$/BFO nanowire arrays, which is beneficial for reducing the reflection of light, enhancing the trapping effect, and improving the light absorption; thus, the light absorption performance of the TiO$_2$/BFO composite nanowire arrays is greater than that of BFO-based thin film materials.

The bandgap can be calculated using the Tauc equation[22]

$$(\alpha h\nu) = B\left(h\nu - E_g\right)^{\frac{1}{2}} \qquad (1)$$

where $h\nu$ is the energy of the incident photon, α is the absorption coefficient, B is a constant related to the material, and E_g is the bandgap.[22,23] In addition, $\alpha = -\frac{\ln T}{d}$, where d is the thickness of the layer and T is the light transmittance of the layer.[23] As shown in Fig. 7b and d, the calculated bandgaps of TiO$_2$ and TiO$_2$/BFO nanowire arrays are 3.16 eV and 2.05 eV, respectively.

PV Performance

After covering the top electrode (graphene), a solar cell test system was used to characterize the PV performance; the results are shown in Fig. 8. The fill factor (FF) was calculated using Eq. 2:[24]

$$FF = \frac{P_{max}}{I_{sc}V_{oc}} \qquad (2)$$

where P_{max}, V_{oc}, and I_{sc} are the maximum output power, open-circuit voltage, and short-circuit current, respectively. The PCE was calculated using Eq. 3:

$$PCE = \frac{J_{sc} \times V_{oc} \times FF}{P_{in}} \times 100\% \qquad (3)$$

where J_{sc} is the short-circuit current density, and P_{in} is the incident light intensity (100 mW/cm^2). Figure 8a shows the J–V curves of a representative sample. It can be seen that the PV effect of TiO$_2$/BFO under light illumination is very obvious. However, it is inconspicuous in the dark. The values of V_{oc}, J_{sc}, FF, and PCE for the TiO$_2$/BFO nanowire arrays under light and dark conditions are listed in Table I.

Figure 8b shows a box diagram of the PCE of the TiO$_2$/BFO nanowire arrays, which indicates that the PV experiment has good reproducibility. Figure 8b shows that the data are relatively scattered, mainly due to small differences in the structures (e.g., thickness) of BFO owing to normal deviations in the preparation process parameters (e.g., the start time of spin coating of BFO), where the maximum, minimum, and average values are 0.1316%, 0.1088%, and 0.1198%, respectively, and the positive and negative errors are within 10% of the available data.

Table II summarizes the five BFO-based ferroelectric PV devices and their PV parameters (J_{sc}, V_{oc}, FF, and PCE). By comparing previously reported BFO thin film-based PV devices such as Au/BFO/ITO,[25] Pt/BFO/ITO,[26] and NSTO/BFO$_{001}$/AZO,[27] we observed that NSTO/BFO$_{001}$/AZO has a higher PCE of 0.0167%, and our FTO/TNAs/BFO/graphene has a PCE of 0.1177%. Thus, the efficiency was improved by 604.79%. Therefore, the composite PCE, V_{oc}, J_{sc}, and FF of TiO$_2$/BFO significantly increased compared to the BFO-based materials, mainly because of the reduced reflection, enhanced light absorption, increased carrier transport efficiency, and reduced recombination of non-radiative composites with the help of nanowire arrays.

Table I V_{oc}, J_{sc}, FF, and PCE of TiO$_2$/BFO nanowire arrays under light and dark conditions

Test conditions	V_{oc} (V)	J_{sc} (mA/cm^2)	FF	PCE (%)
Dark	0.7153	0.0070	0.0026	1.5720×10^{-6}
Light	0.8576	0.2015	0.6811	0.1177

Table II PV parameters of BFO-based solar cells reported in this paper and other BFO thin film structure cells in the literature[25–28]

Devices	J_{sc} (mA/cm^2)	V_{oc} (V)	FF (%)	PCE (%)	Ref
FTO/TNAs/BFO/graphene	0.2015	0.8576	68.11	0.1177	This study
Au/BFO/ITO	0.060	0.20	–	0.0005	25
Pt/BFO/ITO	–	0.1277		0.000024	26
NSTO/BFO$_{001}$/AZO	0.03595	1.31	29.24	0.0167	27
Corning glass/ITO/BFO/Au	0.01337	0.007	–	0.00014	28

Interfacial Carrier Behavior

Further, we characterized TRPL to analyze the carrier lifetime of the TiO_2/BFO core–shell nanowire arrays.

The TRPL intensity decay curve and the corresponding fitting curves are shown in Fig. 9. The fitting formula is a three exponential decay function:[29]

$$y = y_0 + A_1 e^{-x/\tau_1} + A_2 e^{-x/\tau_2} + A_3 e^{-x/\tau_3} \tag{4}$$

The average life is calculated using Eq. 5:

$$\tau_{avg} = \frac{A_1 \tau_1^2 + A_2 \tau_2^2 + A_3 \tau_3^2}{A_1 \tau_1 + A_2 \tau_2 + A_3 \tau_3} \tag{5}$$

where τ_1 and τ_3 represent the fragmentation of photogenerated carriers at the interface, τ_2 is the recombination of carriers assisted by traps inside the ferroelectric absorption layer, and A_1, A_2, and A_3 are the relative amplitudes of these three terms.[29] The corresponding fitting parameters are listed in Table III.

The calculated lifetime is 3.57 ns, which is smaller than the lifetime (6.62 ns) of the BFO film without an ETL reported in the literature.[30] The carrier lifetime length in this study depends mainly on two stages: the rate of electron–hole complexation and the rate of electron–hole separation followed by transport. Through PCE tests, we observed that the V_{oc}, PCE,
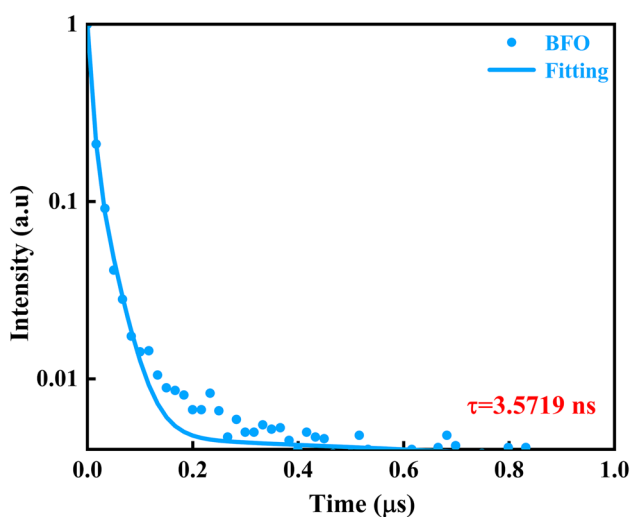
Fig. 9 Carrier fluorescence lifetime plots of TiO_2/BFO core–shell nanowire arrays.

etc., were improved, indicating that the extraction speed of electron–hole was accelerated and the speed of electron–hole compounding decreased. Therefore, in this study, the ETL, TiO_2, played the role of fast carrier transport and enhanced the extraction of the interfacial charge capacity.

Energy Band Structure

In order to understand the effect of energy band alignment after the contact between BFO and TiO_2 nanowire arrays, the "onset" position of the valence band edge binding energy (E_{onset}) and secondary electron cutoff edge binding energy (E_{cutoff}) of BFO and TiO_2 were determined using UPS, and the results are shown in Fig. 10. Meanwhile, the work function (Φ), the valence band maximum binding energy (E_v), and the conduction band minimum binding energy (E_c) were obtained by the following equations:[31]

$$h\nu - \phi = E_{cutoff} - E_F \tag{6}$$

$$E_v = -\phi - E_{onset} \tag{7}$$

$$E_c = E_v + E_g \tag{8}$$

where h is Planck's constant, ν is the frequency of the irradiated light, and $h\nu = 21.22$ eV (energy of the light source of He I). E_F is the Fermi energy level (the calibrated E_F is 0).

Based on the data in Fig. 10, we calculated the E_v and E_c and plotted the energy band diagrams as shown in Fig. 11. Figure 11a shows the energy band diagrams of TiO_2 and BFO before contact, and Fig. 11b illustrates the energy band diagram and direction of electron–hole transfer in the TiO_2/BFO nanowire arrays under illumination.

Under equilibrium conditions, the E_F of TiO_2 and BFO merge into a single energy level. When light is illuminated onto the sample, photons are mainly absorbed by the BFO layer, causing the absorbing layer, BFO, to produce electron–hole pairs, which are separated by the electric field built in the ferroelectric material and driven by the electric field at the heterojunction interface.[19,32,33]

The electrons in the conduction band (CB) of BFO drift toward the CB of TiO_2, driven by the electric field force and axially through the nanowire array to the bottom electrode (FTO). Similarly, the holes in the valence band of BFO move toward the outer electrode, thus limiting the probability of electron–hole recombination. Thus, the overall suppression of the electron–hole recombination probability contributes to the improvement in the photocurrent conversion efficiency of
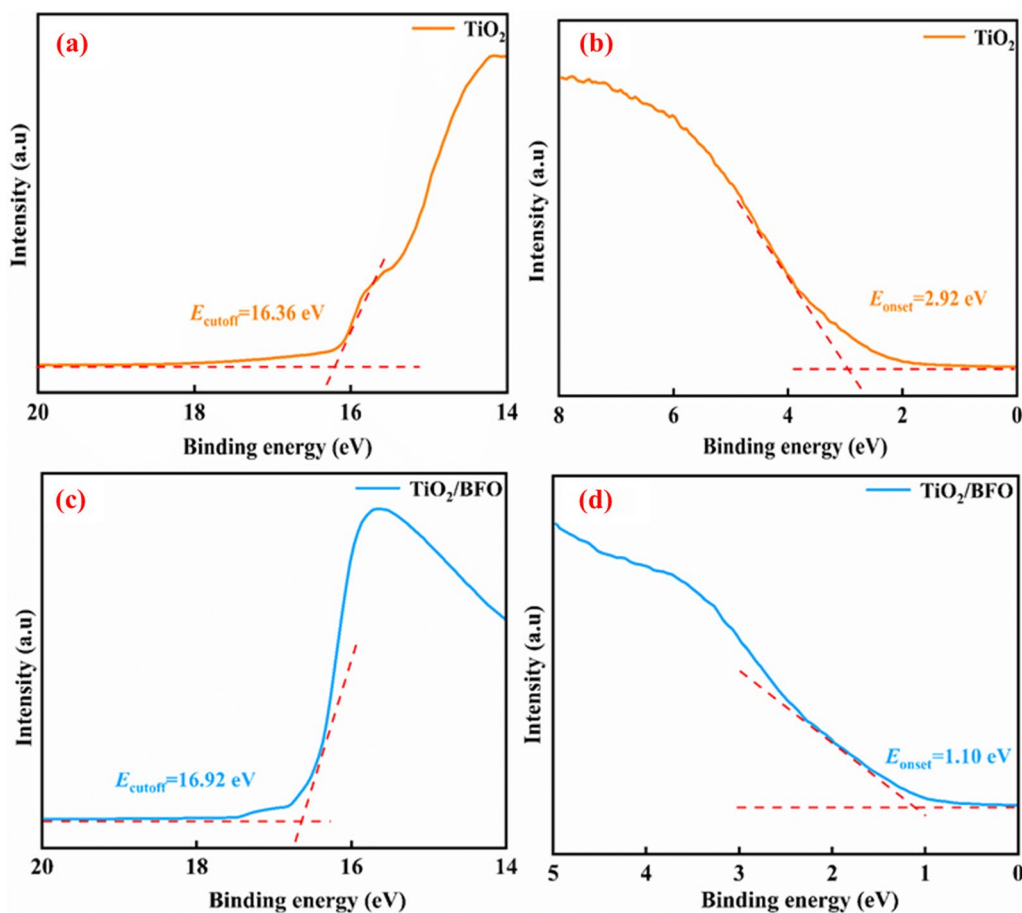
Table III Fitting parameters of the decay curve of TRPL

Sample	A_1	τ_1(ns)	A_2	τ_2(ns)	A_3	τ_3(ns)	τ_{avg}(ns)
TiO_2/BFO	0.6663	1.2161	0.2776	0.0389	0.0537	8.0667	3.5719

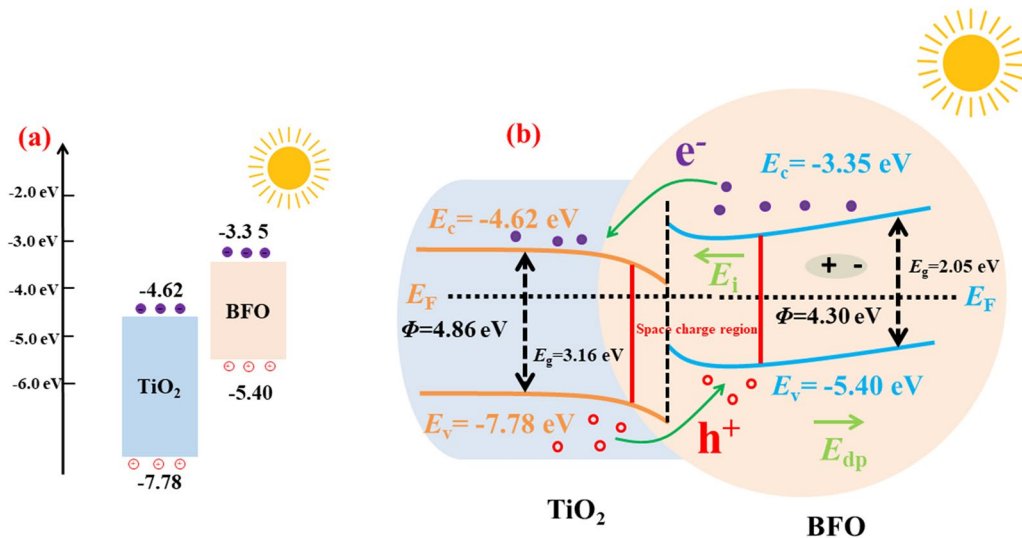**Fig. 10** UPS diagrams of TiO$_2$ (a, b) and TiO$_2$/BFO (c, d).

Fig. 11 (a) and (b) energy band diagrams of the TiO$_2$/BFO core–shell nanowire arrays before and after contact.

the heterojunction devices. In summary, the enhanced light absorption and good carrier transport properties of TiO$_2$/BFO nanowire arrays are responsible for the improvement in PCE.

Conclusion

This study proposes core–shell nanowire arrays of transport materials/ferroelectric materials (such as TiO$_2$/BFO) and confirms that this structure has excellent PV performance. The current PCE of the TiO$_2$/BFO nanowire array solar cells is approximately 0.1177%, which is higher than most reported BFO-based PV devices. UV–Vis spectroscopy, TRPL, energy band diagrams, and J–V curves show that the core–shell structure of the nanowire array can reduce light reflection, enhance light absorption, accelerate carrier transport, and reduce carrier complexation, consequently improving the PCE of BFO. This study demonstrates that the transport material/ferroelectric material core–shell nanowire array structure has excellent PV performance, suggesting a pathway for the enhancement of ferroelectric PV performance.

Author Contributions All authors contributed to the study's conception and design. Material preparation and data analysis are performed by JL, JH, and SL. Data collection is performed by YR, KD, SX, YH, RG, and CF. All authors commented on previous versions of the manuscript. All authors read and approved the final manuscript.

Data Availability The datasets generated during and/or analyzed during the current study are available from the corresponding author on reasonable request.

Conflict of interest On behalf of all authors, the corresponding author states that there is no conflict of interest. We declare that we have no financial and personal relationships with other people or organizations that can inappropriately influence our work, and there is no professional or other personal interest of any nature or kind in any product, service, and/or company that could be construed as influencing the position presented in, or the review of, the manuscript entitled "Microstructures and photovoltaic properties of TiO$_2$/BiFeO$_3$ core–shell nanowire arrays".

Ethical Approval No human and/or animal studies are involved.

References

1. X. Han, Y. Ji, and Y. Yang, Ferroelectric photovoltaic materials and devices. *Adv. Funct. Mater.* 32, 2109625 (2021).

2. X. Zhao, K. Song, H. Huang, W. Han, and Y. Yang, Ferroelectric materials for solar energy scavenging and photodetectors. *Adv. Opt. Mater.* 10, 2101741 (2021).

3. J.J. Yoo, G.Y. Seo, M.R. Chua, T.G. Park, Y.L. Lu, F. Rotermund, Y.K. Kim, C.S. Moon, N.J. Jeon, J.P. Correa-Baena, V. Bulović, S.S. Shin, M.G. Bawendi, and J.W. Seo, Efficient perovskite solar cells via improved carrier management. *Nature* 590, 587 (2021).

4. S.Y. Yang, J. Seidel, S.J. Byrnes, P. Shafer, C.H. Yang, M.D. Rossell, P. Yu, Y.H. Chu, J.F. Scott, J.W. Ager, L.W. Martin, and R. Ramesh, Above-bandgap voltages from ferroelectric photovoltaic devices. *Nat. Nanotechnol.* 5, 143 (2010).

5. R.K. Katiyar, Y. Sharma, P. Misra, V.S. Puli, S. Sahoo, A. Kumar, J.F. Scott, G. Morell, B.R. Weiner, and R.S. Katiyar, Studies of the switchable photovoltaic effect in co-substituted BiFeO$_3$ thin films. *Appl. Phys. Lett.* 105, 172904 (2014).

6. Z.X. Lu, P.L. Li, J.G. Wan, Z.F. Huang, G. Tian, D.F. Pan, Z. Fan, X.S. Gao, and J.M. Liu, Controllable photovoltaic effect of microarray derived from epitaxial tetragonal BiFeO$_3$ films. *ACS Appl. Mater. Inter.* 9, 27284 (2017).

7. C. Godau, T. Kämpfe, A. Thiessen, L.M. Eng, and A. Haußmann, Enhancing the domain wall conductivity in lithium niobate single crystals. *ACS Nano* 11, 4816 (2017).

8. G. Chen, J. Chen, W.J. Pei, Y.M. Lu, Q.F. Zhang, Q. Zhang, and Y.B. He, Bismuth ferrite materials for solar cells: current status and prospects. *Mater. Res. Bull.* 110, 39 (2018).

9. S.J.K. Srivastava, D. Kumar, P.K. Singh, M. Kar, V. Kumar, and M. Husain, Excellent antireflection properties of vertical silicon nanowire arrays. *Sol. Energy Mater Sol. Cells.* 94, 1506 (2010).

10. B. Ozdemir, M. Kulakci, R. Turan, and H.E. Unalan, Effect of electroless etching parameters on the growth and reflection properties of silicon nanowires. *Nanotechnology* 22, 155606 (2011).

11. J.Y. Jung, Z.Y. Guo, S.W. Jee, H.D. Um, K.T. Park, and J.H. Lee, A strong antireflective solar cell prepared by tapering silicon nanowires. *Opt. Express.* 18, A286 (2010).

12. Y.J. Wang, J.L. Qu, and Q. Wen, CH$_3$NH$_3$PbI$_3$ perovskite with enhanced absorption and stability using silver nanowires and the anatase structure of TiO$_2$ nanowires. *J. Electron. Mater.* 51, 778 (2022).

13. O.L. Muskens, S.L. Diedenhofen, B.C. Kaas, R.E. Algra, E.P.A.M. Bakkers, J.G. Rivas, and A. Lagendijk, Large photonic strength of highly tunable resonant nanowire materials. *Nano Lett.* 9, 930 (2009).

14. L. Wen, Z.F. Zhao, X.H. Li, Y.F. Shen, H.M. Guo, and Y.Q. Wang, Theoretical analysis and modeling of light trapping in high efficiency GaAs nanowire array solar cells. *Appl. Phys. Lett.* 99, 143116 (2011).

15. Y.L. Wang, J.W. Wan, J. Ding, J.S. Hu, and D. Wang, Rutile TiO$_2$ electron transport layer for the enhancement of charge collection for efficient perovskite solar cells. *Angew. Chem. Int. Edit.* 58, 9414 (2019).

16. A.S. Zhu, Q.D. Zhao, X.Y. Li, and Y. Shi, BiFeO$_3$/TiO$_2$ nanotube arrays composite electrode: construction, characterization, and enhanced photoelectrochemical properties. *ACS Appl. Mater. Interfaces.* 6, 671 (2014).

17. P. Joshna, A. Hazra, K.N. Chappanda, P.K. Pattnaik, and S. Kundu, Fast response of UV photodetector based on Ag nanoparticles embedded uniform TiO$_2$ nanotubes array. *Semicond. Sci. Technol.* 35, 2 (2020).

18. X.S. Cao, J.M. Wu, Z. Zhang, J.Y. Qin, Z.G. Fu, J.H. Hai, Z.C. Wang, Z.Z. Ye, and W. Wen, Electrochemical lithium

intercalation in titania nanowire arrays for boosting photocatalytic activity. *J. Electron. Mater.* 52, 23 (2023).

19. H. Renuka, S. Sharma, B.H. Venkataraman, K. Ramaswamy, K.N. Chappanda, S. Kundu, and S. Goel, Extensive enhancement in charge collection efficiency of ferroelectric Cr-Doped BFO-based solar cells by Using TiO$_2$ Nanotube Arrays. *IEEE J. Photovolt.* 11, 1278 (2021).

20. A. Srivastava, A. Awale, M. Vashista, and M.Z.K. Yusufzai, Monitoring of thermal damages upon grinding of hardened steel using Barkhausen noise analysis. *J. Mech. Sci. Technol.* 34, 2145 (2020).

21. S.R. Jhang, H.Y. Lin, Y.S. Liao, J.P. Chou, and J.M. Wu, Local dipole enhancement of space-charge piezophototronic catalysts of core-shell polytetrafluoroethylene@TiO$_2$ nanospheres. *Nano Energy* 102, 107619 (2022).

22. X.L. Liang and J.Q. Dai, Prominent ferroelectric properties in Mn-doped BiFeO$_3$ spin-coated thin films. *J. Alloys Compd.* 886, 161168 (2021).

23. C. Chen, J. Su, and G.L. Song, Effect of Ca^{2+} doping on structure and optical properties in multiferroic BiFeO$_3$ thin Films. *J. Henan Norm. Univ. Nat. Sci. Ed.* 42, 60 (2021).

24. Z.H. Fu, J.C. Zhang, X.Y. Yang, and W.L. Cao, Preparation of nano-crystal N-Zn/TiO$_2$ anode films and the effects of co-sensitization on the performance of dye-sensitized solar cells. *Sci. Bull.* 56, 2001 (2011).

25. L. Huang, M. Wei, C. Gui, and L.J. Jia, Ferroelectric photovoltaic effect and resistive switching behavior modulated by ferroelectric/electrode interface coupling. *J. Mater. Sci. Mater. Electron.* 31, 20667 (2020).

26. R. Arti, S.P. Gupta, R. Singh, V. Walia, and V. Kumar, Verma, Modification in photovoltaic and photocatalytic properties of bismuth ferrites by tailoring band-gap and ferroelectric properties. *J. Alloys Compd.* 908, 164602 (2022).

27. Y. Chen, H.M. Wei, M.X. Wang, and B.Q. Cao, Enhancing the bulk photovoltaic effect by tuning domain walls in epitaxial BiFeO$_3$ films. *Nanotechnology* 32, 495402 (2021).

28. S. Ameer, K. Jindal, M. Tomar, A. Kumar, P.K. Jha, and V. Gupta, A theoretical and experimental formalism of electronic structure of BFO: Cr thin films and modulation of their electrical properties upon visible light illumination. *J. Appl. Phys.* 124, 155304 (2018).

29. H. Bi, X. Zuo, B.B. Liu, D.M. He, L. Bai, W.Q. Wang, X. Li, Z.Y. Xiao, K. Sun, Q.L. Song, Z.G. Zang, and J.Z. Chen, Multifunctional organic ammonium salt-modified SnO$_2$ nanoparticles toward efficient and stable planar perovskite solar cells. *J. Mater. Chem. A.* 9, 3940 (2021).

30. D.W. Cao, M. Li, J.F. Zhu, Y.F. He, T. Chen, Y. Liu, M.M. Chen, and Y. Yang, Enhancement of photoelectrochemical performance in ferroelectric films via the introduction of an Au buffer layer. *J. Semicond.* 42, 112701 (2021).

31. Y.F. He, S.L. Xin, Y. Ren, S.S. Li, J.Z. He, J.H. Li, and C.L. Fu, Effects of anti-solvent temperature on microstructures and photovoltaic properties of TiO$_2$@MAPbI$_3$ core-shell nanowire arrays. *Physica E Low Dimens. Syst. Nanostruct* 147, 11560 (2023).

32. T.T.Y. Tan, C.K. Yip, D. Beydoun, and R. Amal, Effects of nano-Ag particles loading on TiO$_2$ photocatalytic reduction of selenate ions. *Chem. Eng. J.* 95, 179 (2003).

33. S.J. Clark and J. Robertson, Band gap and Schottky barrier heights of multiferroic BiFeO$_3$. *Appl. Phys. Lett.* 90, 132903 (2007).